Voltammetric study of the affinity of divalent heavy metals for guanine functionalized iron oxide nanoparticles

Simona Sawan [1,2] ● Khalil Hamze [3] ● Ali Youssef [3] ● Rayyan Boukarroum [2] ● Kamal Bouhadir [3] ● Abdelhamid Errachid [1] ● Rita Maalouf [2] ● Nicole Jaffrezic-Renault [1]

Received: ……/Accepted …

Abstract In this study, a novel nanobiomaterial based on (3-aminopropyl)triethoxysilane (APTES) coated iron oxide (Fe_3O_4) nanoparticles functionalized with newly synthesized guanine hydrazide (GH) was elaborated. A boron-doped diamond electrode coated with GH-APTES-Fe_3O_4 nanoparticles was used to assess the interaction of heavy metal ions with guanine hydrazide. The adsorption isotherms were electrochemically investigated and it was shown that the adsorption capacity of the nanoparticles towards heavy metals decreased in the following order: Cu^{2+}>Pb^{2+}>Cd^{2+}. From the calibration curves, the sensitivities of detection were as follows: 171.6 µA/µM for Cu (II), 156 µA/µM for Pb (II) and 101.4 µA/µM for Cd (II).

Keywords Nucleosides ● Heavy Metals ● Nanostructures ● Electrochemistry ● Metal complexes

✉ Nicole Jaffrezic-Renault

nicole.jaffrezic@univ-lyon1.fr

[1] University of Lyon, Institute of Analytical Sciences, 5, rue de la Doua, 69100 Villeurbanne, France

[2] Department of Sciences, Faculty of Natural and Applied Sciences, Notre Dame University - Louaize, Zouk Mosbeh, Lebanon.

[3] Department of Chemistry, American University of Beirut, Beirut 11-0236, Lebanon.

Introduction

Despite the many uses of heavy metals, excessive exposure, either externally or by ingestion, can be harmful to humans, animals and plants on several levels. They are nonbiodegradable and thus have the tendency to accumulate in living organisms. Besides being considered as environmental pollutants [1], some heavy metals can cause skin, liver, kidney, bone and neurological diseases [2]. Along with natural sources, heavy metals can be released from industrial sources such as fertilizers, household waste, cosmetics, paint, batteries and plastics [3]. The range of toxicity of heavy metals depends on several factors including their charges, concentrations, way of exposure…

Although the main function of nucleic acids is encoding genetic information in human beings, they have been widely explored in the fields of catalysis and ligand binding [4]. Nucleic acids are known to have different metal binding sites, binding capacity and affinity for heavy metals [5]. For years, the interaction of metal cations with nucleic acids has been investigated. It was noted that metal ions impact differently the stability and structure of nucleic acids depending on the type and concentration of metal ion and its relative affinity to the phosphate and nucleobases. It has been hypothesized that bioavailable metal ion-induced toxicity inactivates vital processes, inhibits metabolic pathways and directly or indirectly displaces

essential metals from the active sites of macromolecules and/or disrupts depolymerization or repair of nucleotide bases with subsequent errors in protein synthesis [6]. The study of the interaction between nucleic acids and heavy metal ions can help explain their biotoxicity mechanisms, and these interactions can be used for the detection of toxic heavy metals in waters. Recently, nucleic acids, nucleotides, nucleosides, nucleobases and their derivatives have been gaining wide popularity in heavy metal sensing [7]. They are biodegradable, highly selective and can be produced by natural or synthetic methods. Many studies have relied on the stabilization or destabilization of G-quadruplex structure of guanine-rich DNA, formation of stable base pairs or catalytic cleavage of DNA substrates for the detection of heavy metals [8].

Among the five natural nucleobases, guanine and its derivatives have received considerable interest [9]. Guanine is a purine derivative that consists of a fused pyrimidine-imidazole ring system with conjugated double bonds. It has been well established that metal ions bind to the carbonyl oxygen O(6) and/or the imidazolyl nitrogen N(7) of guanine. Preference of the binding site depends on the metal ion itself [10]. In the present work, the voltametric behavior of guanine in the presence of divalent heavy metal ions was studied. It is known that the redox moiety of guanine is the imidazolyl nitrogen N(7) [11]. The interaction of N(7) with heavy metal ions can then

be monitored through the change of the electron transfer rate. For the sensitive detection of the oxidation of guanine, synthesized guanine hydrazide (GH) was immobilized on iron oxide nanoparticles that present a large specific surface area and a high electrical conductivity. Recently, magnetic nanoparticles, particularly magnetite Fe_3O_4 nanoparticles, have attracted a lot of interest owing to their unique properties of superparamagnetism, low Curie temperature, high magnetic susceptibility, low toxicity and cost effectiveness [12,13]. The exclusive magnetic and electrical properties are the result of the transfer between Fe^{2+} and Fe^{3+} [14]. They have a wide variety of applications ranging from environmental to biological and medical. Synthesis conditions are crucial in determining their size and physicochemical properties, and thus several processes have been investigated for their production depending on the desired application. Moreover, Fe_3O_4 nanoparticles have the tendency to aggregate due to magnetic dipole-dipole interactions between particles [15], which is why in most electrochemical studies they are either coated or functionalized [16]; i.e. iron oxide core encapsulated in an organic or inorganic shell [17]. Owing to their versatile properties, Fe_3O_4 nanoparticles were extensively used in combination with biological recognition elements such as enzymes, antibodies and nucleic acids for various applications [18]. The guanine functionalized iron oxide nanoparticles were immobilized on the surface of

a boron doped diamond (BDD) electrode. BDD electrodes are extensively investigated for electroanalytical applications, because of their electrochemical properties, as a low background current and a wide potential window in aqueous solutions (~−1.35 to +2.3 V versus the normal hydrogen electrode), corrosion stability in aggressive media and resistance to biofouling [19]. The redox properties of guanine were detected in the presence of copper, lead and cadmium ions. From these results, adsorption of the three heavy metals on N(7) site of guanine was characterized and the sensitive electrochemical detection of these heavy metal could then be achieved. This study aims to show that the use of the proposed guanine functionalized nanoparticles associated with a voltammetric technique could present a great potential in the physico-chemical characterization of the guanine/metal interaction.

Results and Discussion

Guanine hydrazide preparation and characterization

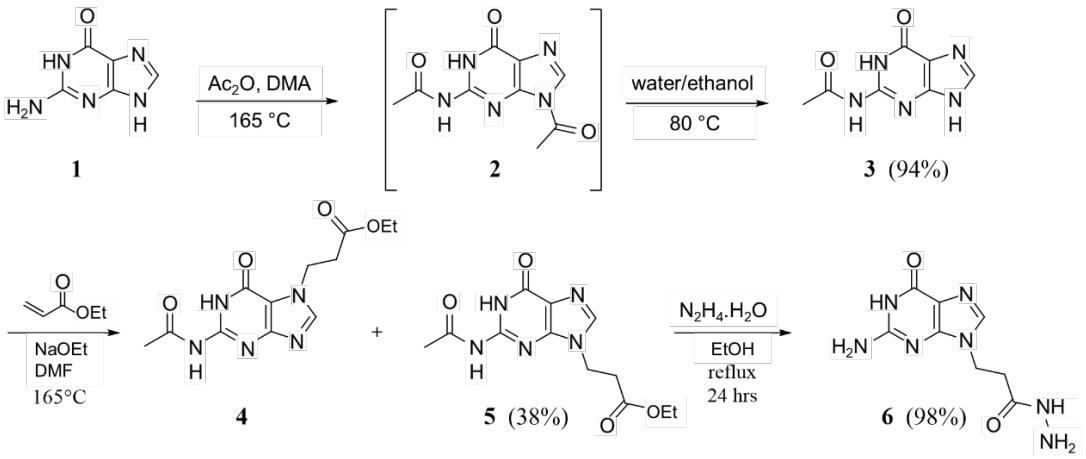

Fig. 1 Schematic diagram showing the steps of guanine hydrazide synthesis

Figure 1 summarizes the overall steps involved in the synthesis of *3-(2-amino-6-oxo-1,6-dihydro-9H-purin-9-yl)propane hydrazide* (**6**, $C_8H_{10}N_7O_2$) or guanine hydrazide. The process of guanine hydrazide synthesis generated a white product with a yield of 98%. To prepare the guanine hydrazide **6** shown in figure 1, The exocyclic amine of guanine **1** was first protected by acetylation according to literature procedure [21]. Then reaction of N^2-acetylguanine **3** via a Michael addition with Ethyl acrylate and sodium ethoxide afforded, as expected, a mixture of two isomeric ethyl propionates resulting from guanine alkylation at either the N-9 (**5**) or N-7 (**4**) atom. These compounds were separated by Flash chromatography and, after their structural assignment, the reaction of the N-9 ester with hydrazine hydrate in ethanol led to the formation of the desired acyl hydrazide **6** according to an established literature procedure [22].

The synthesized guanine hydrazide was characterized using FTIR and ^1H and ^{13}C NMR. The infrared spectrum shown in figure 2a revealed peaks at 1695 cm^{-1} corresponding to C=O, 1657 and 3310 cm^{-1} corresponding to NH and 1440 cm^{-1} corresponding to C-N. Peaks at 2854 cm^{-1} correspond to C-H stretching of CH_2 in the hydrazide function, along with a weak peak at 1563 corresponding to C=C stretching. ^1H NMR characterization (500 MHz, DMSO-d_6) showed that the two methylene group protons resonate at 3.36

(triplet, 2H) and 4.14 (triplet, 2H) while the proton from the methine group resonates at 7.54. Protons from the primary amine groups at 4.22 – 4.19 and 6.49 whereas those from secondary amines appear at 9.04 and 10.49 (figure 2b). ^{13}C NMR results in figure 2c are consistent with literature such that the signals corresponding to the guanine carbons appear at 156.8, 153.5, 151.0, 137.4 and 116.5 while those for the hydrazide function appear at 168.7, 39.5 and 33.5 [23].

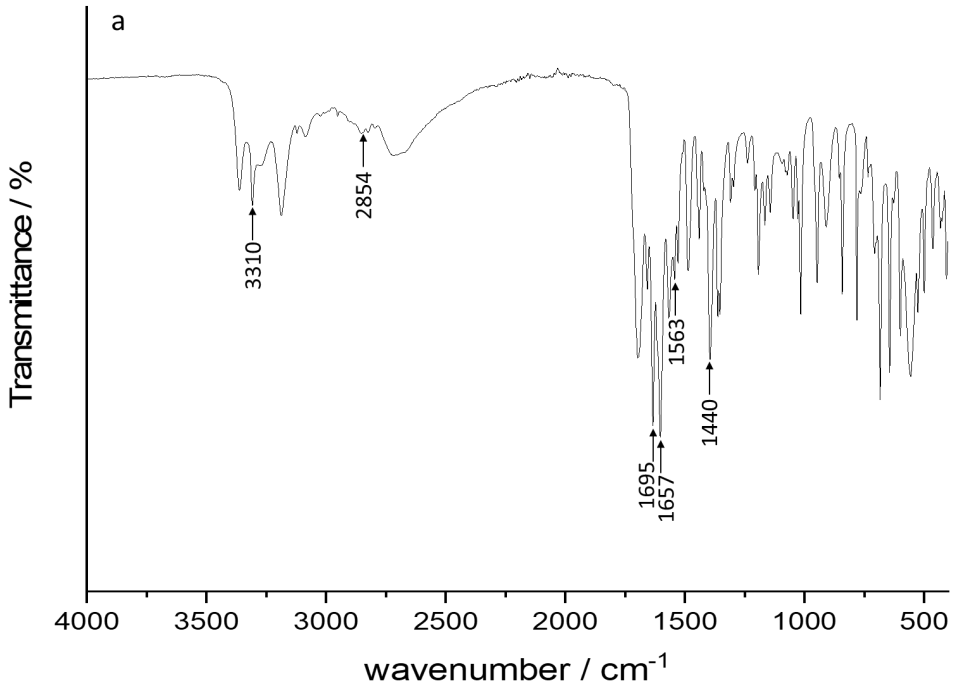

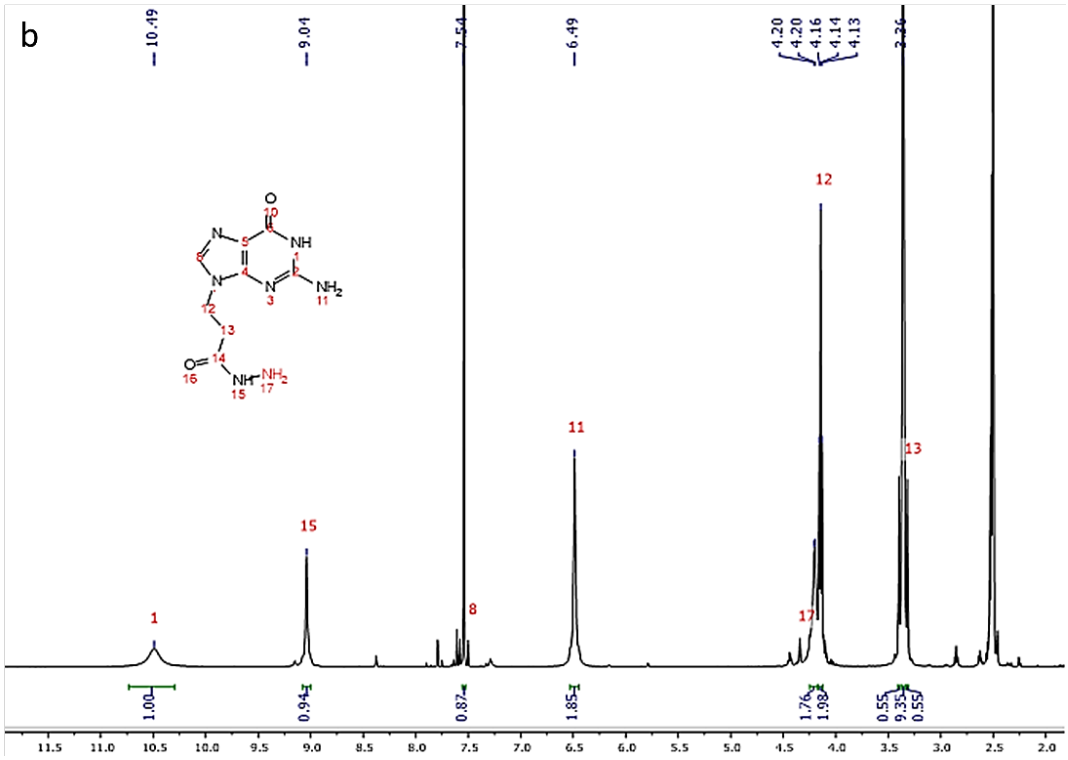
b
10.49
9.04
7.54
6.49
4.20
4.20
4.16
4.14
4.13
3.26
12
11
13
15
1
8
17
1.00
0.94
0.87
1.85
1.76
1.98
0.55
9.35
0.55

1

2

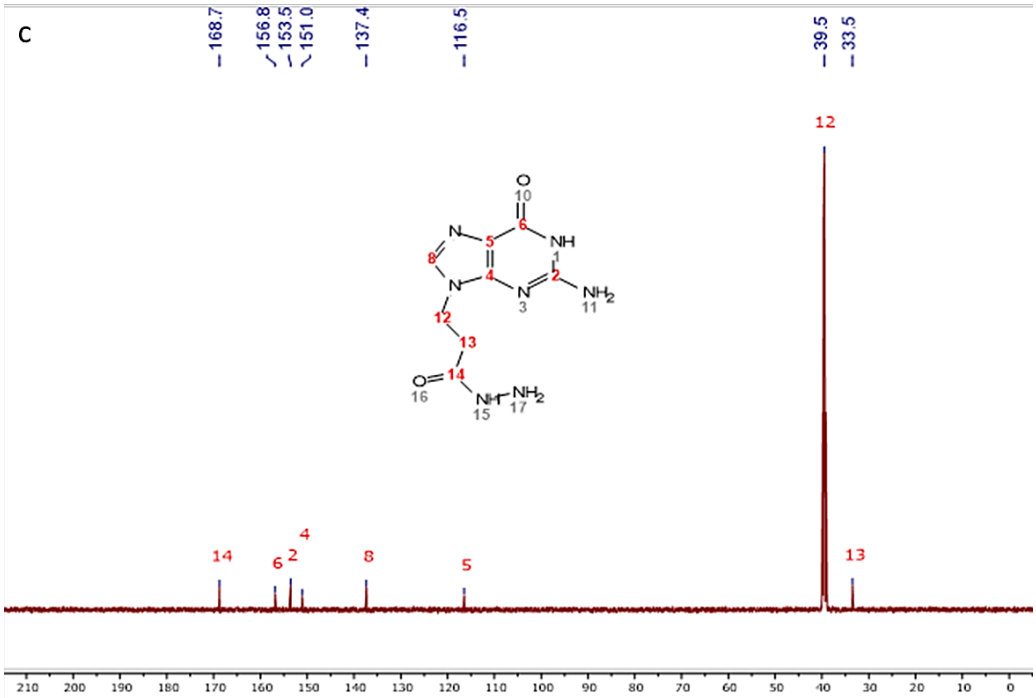
c
168.7
156.8
153.5
151.0
137.4
116.5
39.5
33.5
12
14
4
6
2
8
5
13

3

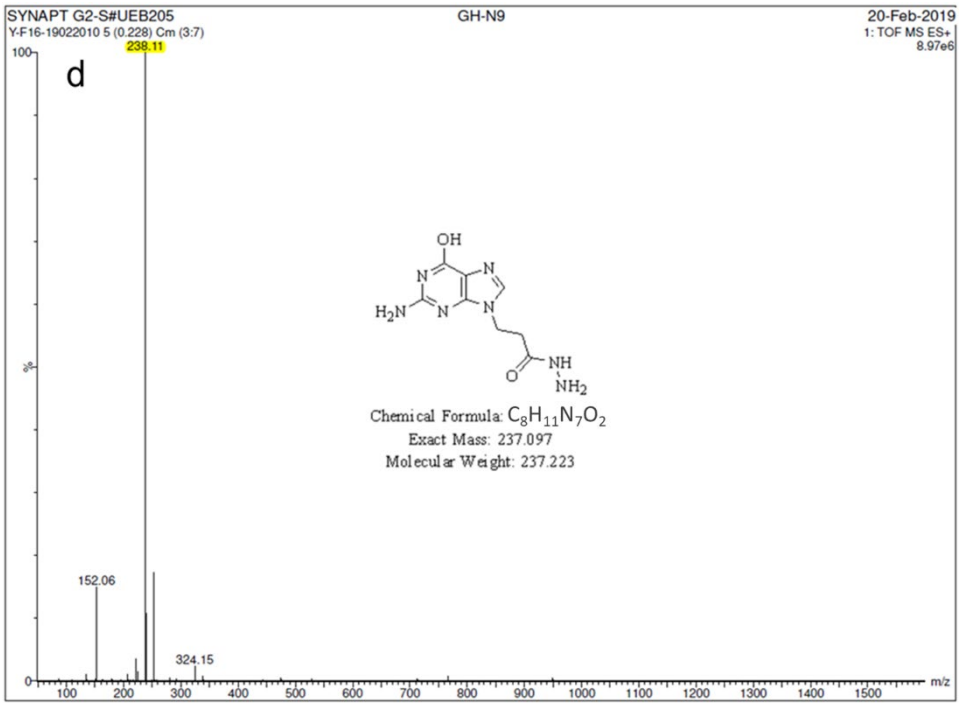

Fig. 2 (a) FTIR spectrum, (b) ^{1}H NMR, (c) ^{13}C NMR and (d) HRMS of guanine hydrazide

Preparation of GH-APTES functionalized Fe_3O_4 nanoparticles

The co-precipitation of ferrous and ferric ions in a basic medium is a classical method for the preparation of Fe_3O_4. The size of the iron oxide nanoparticles directly affects their magnetic properties and should therefore be optimized based on the desired application [13]. Nanoparticles that are too small (less than 20 nm) can't be manipulated by an external magnetic field. Hence, the coprecipitation procedure was carried out at 0 °C to ensure the synthesis of nanoparticles of adequate size. Upon the addition of NaOH, the color of the solution changed gradually from orange to brown to black.

Precipitation of Fe_3O_4 is expected at pH > 7.5 [15]. The reactions involved in the production of Fe_3O_4 are:

$$Fe^{3+} + 3HO^- \rightleftharpoons Fe(OH)_3 \quad (1)$$

$$Fe(OH)_3 \rightleftharpoons FeO(OH) + H_2O \quad (2)$$

$$Fe^{2+} + 2HO^- \rightleftharpoons Fe(OH)_2 \quad (3)$$

$$Fe(OH)_2 + 2FeO(OH) \rightleftharpoons Fe_3O_4 + H_2O \quad (4)$$

The process of amino modification of Fe_3O_4 nanoparticles by direct immobilization of (3-aminopropyl)triethoxysilane on the surface of the nanoparticles can be expected to occur through a silanization reaction, leaving the NH_2 group of APTES exposed. This step is usually very complex and is influenced by several parameters including the reaction time, temperature and silane concentration.

Finally, the functionalization of the APTES-coated nanoparticles with guanine hydrazide was done using glutaraldehyde. The overall reaction for the synthesis of the functionalized electrode is shown in figure 3.

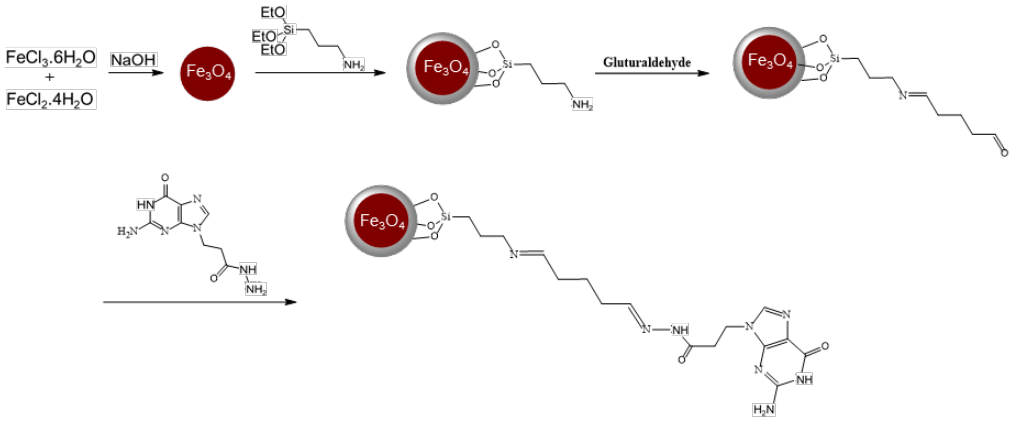

Fig. 3 Schematic diagram showing the process of synthesizing the GH-APTES-Fe_3O_4 nanoparticles

Characterization of the functionalized nanoparticles

FTIR spectroscopy was used to study the functionalization of the bare and coated nanoparticles, as shown in figure 4A. For the bare nanoparticles, one peak at 550 cm^{-1} is noticeable. This peak is the characteristic absorption peak of Fe-O. This band can also be observed with the coated nanoparticles, along with new bands confirming the adsorption of (3-aminopropyl)triethoxysilane on the surface of Fe_3O_4. Bands at 3672 cm^{-1} and 1624 cm^{-1} can be attributed to the N-H stretching and NH_2 bending modes, respectively, of a free NH_2 group. Bands at 1063 cm^{-1} and 1162 cm^{-1} can be attributed to Si-O-Si and SiO-H groups. The stretching of -CH_2 was confirmed with bands at 2902 cm^{-1} and 2973 cm^{-1} [13]. The absorption band corresponding to the Fe-O-Si bond can't be seen since it overlaps with that of Fe-O vibration. However, the shift in the Fe-O band from 550 cm^{-1} to 562 cm^{-1} indicates that there is an Fe-O-Si bond [16]. FTIR measurement after the functionalization of APTES coated nanoparticles with GH confirmed the crosslinking of GH to the APTES by the appearance of new peaks not characteristic of APTES. The shift in the peak corresponding to N-H stretching from 3672 cm^{-1} to 3440 cm^{-1} is consistent with N-H stretching of an amide group along with an increased peak intensity. The -CH_2 stretching

peaks also increased in intensity due to the increased number of CH_2 groups from the hydrazide function.

Powder XRD patterns of the coated nanoparticles show diffraction peaks at 30.1°, 35.4°, 43.1°, 53.4°, 57.0°, and 62.6° corresponding to the characteristic pattern of pure magnetite Fe_3O_4 (figure 4B). The diffraction peaks can be assigned to the (220), (311) (400), (422), (511) and (440) diffraction planes, respectively [17]. This proves that the coating doesn't affect the core magnetite and doesn't lead to a phase change.

The morphology of the prepared nanoparticles capped with (3-aminopropyl)triethoxysilane was investigated using SEM as shown in figure 4C. The magnetic nanoparticles appear to be quasi-spherical, with uniform distribution and an average size of 45 nm. Energy-dispersive X-ray spectroscopy (EDX) was performed to study the elemental composition of the APTES coated Fe_3O_4 nanoparticles (figure 4D). Peaks corresponding to iron (Fe) at about 0.6, 6.3 and 7 keV and oxygen (O) confirm the formation of iron oxide nanoparticles [18]. The presence of peaks corresponding to Si and N confirm that the APTES coating was successful.

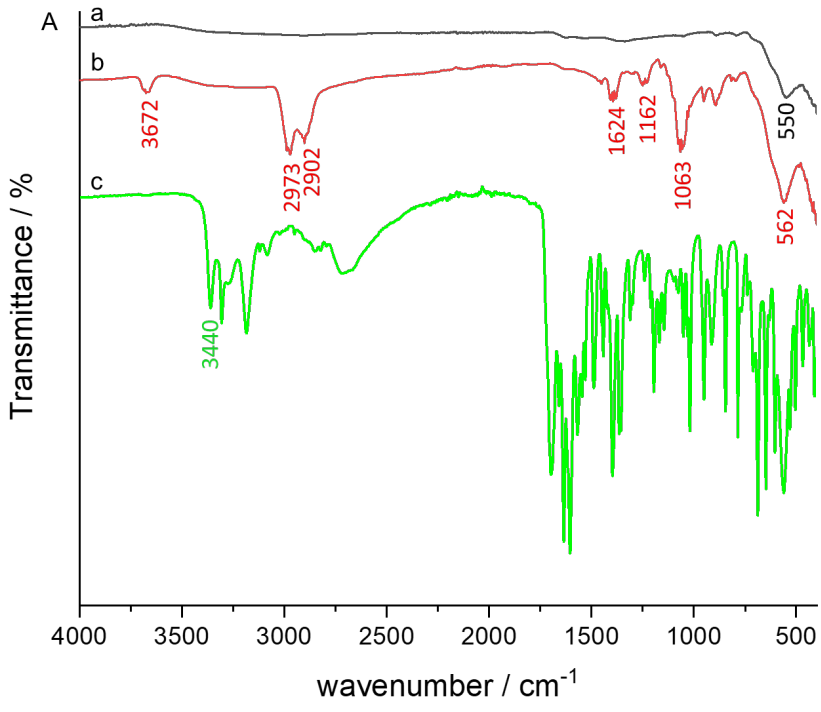
A
a
b
c
3672
2973
2902
1624
1162
1063
550
562
3440
Transmittance / %
4000
3500
3000
2500
2000
1500
1000
500
wavenumber / cm-1

1

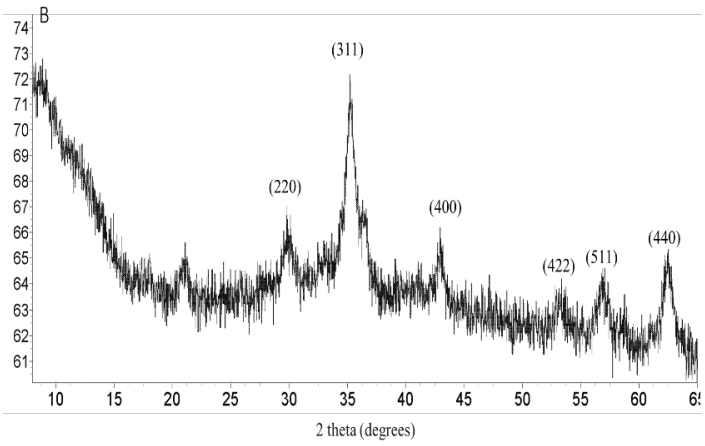
B
(220)
(311)
(400)
(422)
(511)
(440)
2 theta (degrees)

2

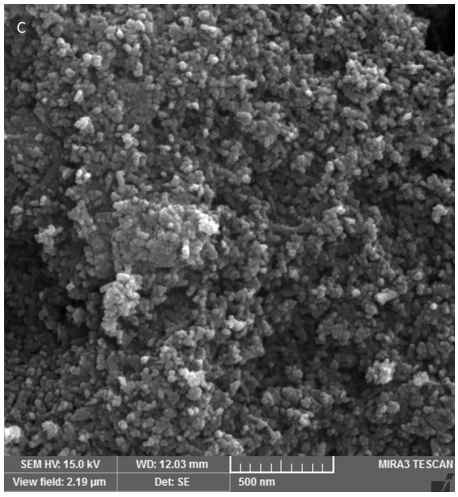

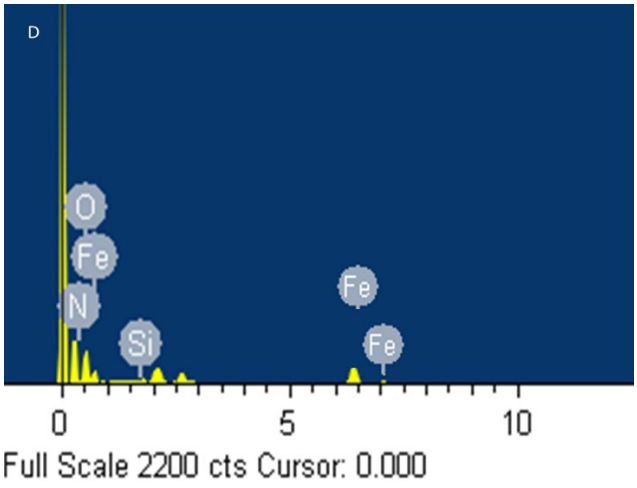

Fig. 4 (A) FTIR spectrum of (a) bare Fe_3O_4 NPs, (b) APTES- Fe_3O_4 NPs and (c) GH-APTES-Fe_3O_4 NPs, (B) XRD pattern, (C) SEM image and (D) EDX spectrum of APTES-Fe_3O_4 nanoparticles

Voltammetric study of the GH-APTES functionalized nanoparticles in the presence of divalent heavy metals

Prior to studying the voltammetric behavioral interaction of heavy metals with the modified electrode, each of the different elements were studied electrochemically to check for their respective signals. As shown in figure 5a, no observable peaks were detected with square wave voltammetry

in the range between -1 and 1.5 V for the BDD electrode coated with APTES-Fe_3O_4 NPs. However, upon functionalization of the nanoparticles with GH, a peak appears at 1.1 V as indicated in figure 5b. This peak is characteristic of the oxidation of guanine at a BDD electrode [11, 24] and not the hydrazide function which is oxidized at a higher potential (1.8 V) [25]. The oxidation reaction of guanine in aqueous media is presented in Fig. 6 [11].

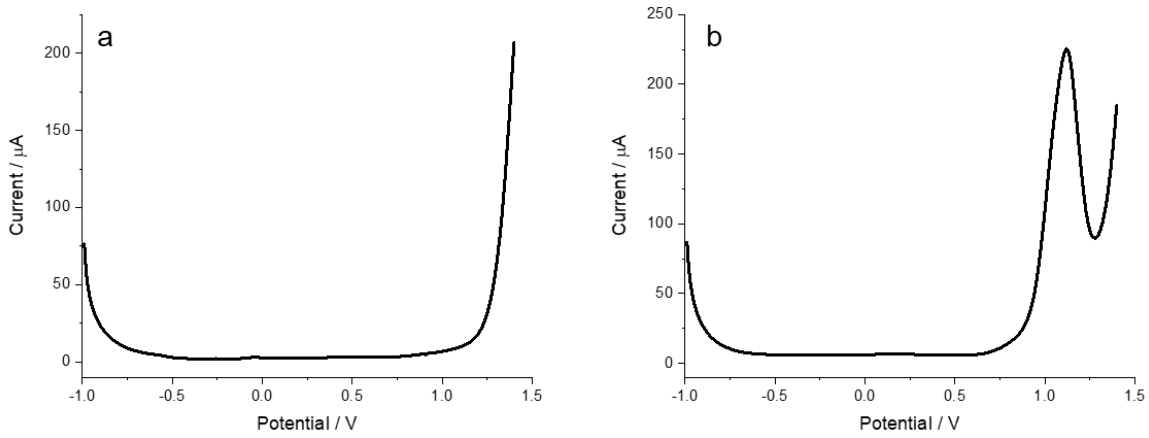

Fig. 5 SWV of (a) APTES-Fe_3O_4 nanoparticles and (b) APTES-Fe_3O_4 nanoparticles functionalized with GH

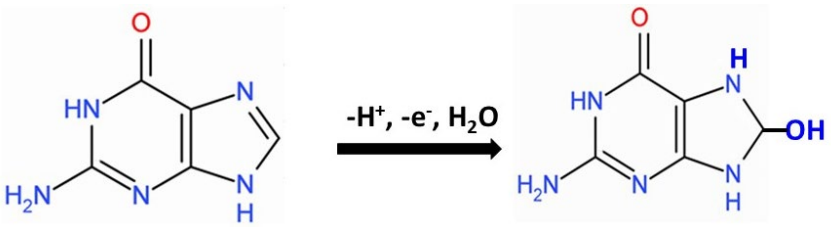

Fig. 6 Oxidation reaction of guanine, in aqueous medium

The effect of Cd (II) ions concentration on the oxidation signal of GH was first investigated after interaction in solution and using a bare BDD (data

not shown). Square wave voltammetry was applied for a solution of GH in citrate buffer (pH 4) with 0.5 mol dm^3 KCl at the following optimized conditions: frequency 50 Hz; amplitude 50 mV; step potential 10 mV. Before adding cadmium, the oxidation peak of GH appeared at 1.1 V. The peak current decreased upon the addition of increasing concentrations of Cd^{2+} implying that the complex formation of cadmium ions with GH hinder the redox reaction of the guanine moiety.

Using a BDD electrode modified with GH functionalized nanoparticles, the same behavior was observed. The intensity of the peak current was found to decrease when the Cd (II) concentration increased. The same behavior was observed with all the studied heavy metal ions. The square wave signals in the presence of the different divalent heavy metals are shown in figure 7.

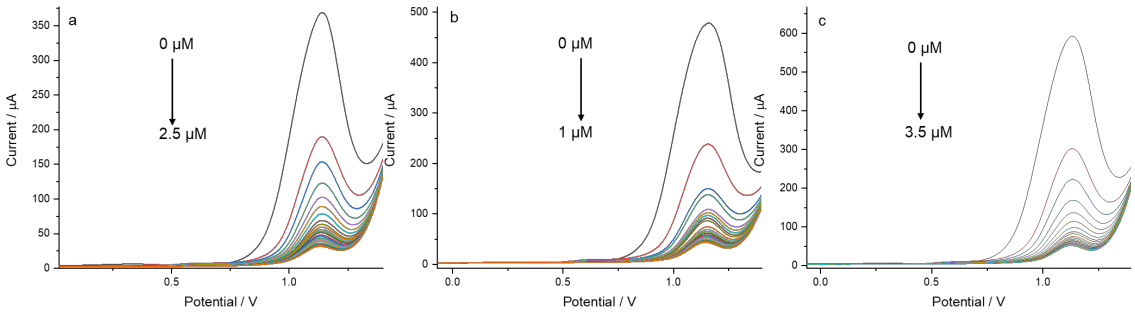

Fig. 7 SWV of (a) Cd (II) at the GH-APTES-Fe_3O_4 NP electrode over a concentration range of 0 – 2.5 µmol dm^{-3}, (b) Pb (II) at the GH-APTES-Fe_3O_4 NP electrode over a concentration range of 0 – 1 µmol dm^{-3} and (c) Cu

(II) at the GH-APTES-Fe_3O_4 NP electrode over a concentration range of 0 – 3.5 μmol dm^{-3}

Adsorption isotherms of the divalent heavy metal ions on the GH-APTES functionalized nanoparticles

In order to characterize the interaction between heavy metals and the functionalized nanoparticles, adsorption isotherms were modeled. Adsorption isotherms are mathematical models describing the distribution of the adsorbate between the solution and the adsorbent. These models are based on to the possibility of interaction between the adsorbate species, type of coverage and the homogeneity/heterogeneity of the adsorbent surface [26]. The variation of the peak maximum (ΔI) (mean value of triplicate) is proportional to the adsorbed concentration of the heavy metals at the modified electrode surface. The adsorption isotherm of the heavy metals was then built from this value, the initial concentration of the heavy metals was not highly modified, due to the small surface area of the modified electrode in contact. Two models were tested: Langmuir and Freundlich.

i. Langmuir isotherm

The Langmuir model assumes that adsorption occurs on a structurally homogeneous adsorbent in a monolayer, or that the adsorption occurs at fixed sites that are identical and energetically equivalent. The linearized form of the Langmuir isotherm can be written as follows [27]:

$$c_e/\Delta I = 1/Q_0 b + c_e/Q_0$$

where Q_0 is the adsorption capacity (μg g^{-1}) and b is the energy of adsorption (L μg^{-1}). Figure 8 shows the Langmuir plot $c_e/\Delta I$ versus c_e for the different heavy metals, each in their respective concentration range. The plots indicate that the experimental data are well fitted with the model with $r^2 > 0.999$. The values of the adsorption capacities were 400, 280.1 and 343.6 $mg.g^{-1}$ for Cu^{2+}, Cd^{2+} and Pb^{2+}, respectively. Moreover, the essential characteristics of the Langmuir model can be expressed as the dimensionless constant separation factor R_L as follows [27]:

$$R_L = 1/(1 + Q_0 b)$$

In the case of the three different metals, R_L falls in the range of 0 – 1 indicating that the nature of the adsorption isotherm is favorable. The adsorption capacity of the functionalized nanoparticles towards the studied heavy metal ions decreases in the following order: $Cu^{2+} > Pb^{2+} > Cd^{2+}$.

ii. Freundlich isotherm

Freundlich isotherm is another form of the Langmuir model describing a heterogeneous system with multiple adsorption sites. The linearized logarithmic form of the Freundlich model can be expressed as follows [28]:

$$\log \Delta I = \log K_F + (1/n) \log c_e$$

where K_F is the Freundlich constant (μg g^{-1}) and n is the Freundlich exponent. The different isotherms for each heavy metal are shown in figure 8 where log ΔI is plotted versus log c_e. It should be noted that the concentration range over which this model was linear was much smaller than that with the Langmuir model for all the studied metal ions. The values of n lie between 1 and 10, which implies that the adsorption is favorable and heavy metals are easily extracted from the solution. This result agrees with the values of R_L from Langmuir's isotherm. Langmuir and Freundlich model parameters and linear regression correlations calculated from curve fittings are shown in Table 1. Better regression correlations were calculated for Langmuir model suggesting that the Langmuir model is more convenient in describing the adsorption process. This signifies that the adsorption is of a typical monomolecular layer form [29]. It assumes that the adsorption is localized, all active sites have similar energies and no interaction between the adsorbed molecules exists [30]. The different affinities and adsorption capacities rely on both the adsorbent (mainly its guanine moiety) and the adsorbate (ionic radius, electronegativity, charge…) [29,31]. Consequently, comparing the divalent metal ions, the orders of affinity and adsorption capacity decrease with increasing ionic radii and electronegativity.

Table 1 Constant parameters and correlation coefficients calculated for different adsorption models for Cu^{2+}, Cd^{2+} and Pb^{2+} adsorption

Isotherm	Langmuir				Freundlich		
Constants	Q_0 (μg g^{-1})	b (L μg^{-1})	R_L	r^2	n	k_F (μg g^{-1})	r^2
Cd^{2+}	280.1	0.087	0.0394	0.9999	6.06	118.2	0.9614
Cu^{2+}	400	0.0707	0.0341	0.9998	5.447	150.7	0.9796
Pb^{2+}	343.6	0.1046	0.0271	0.9999	7.776	174.3	0.9961

1

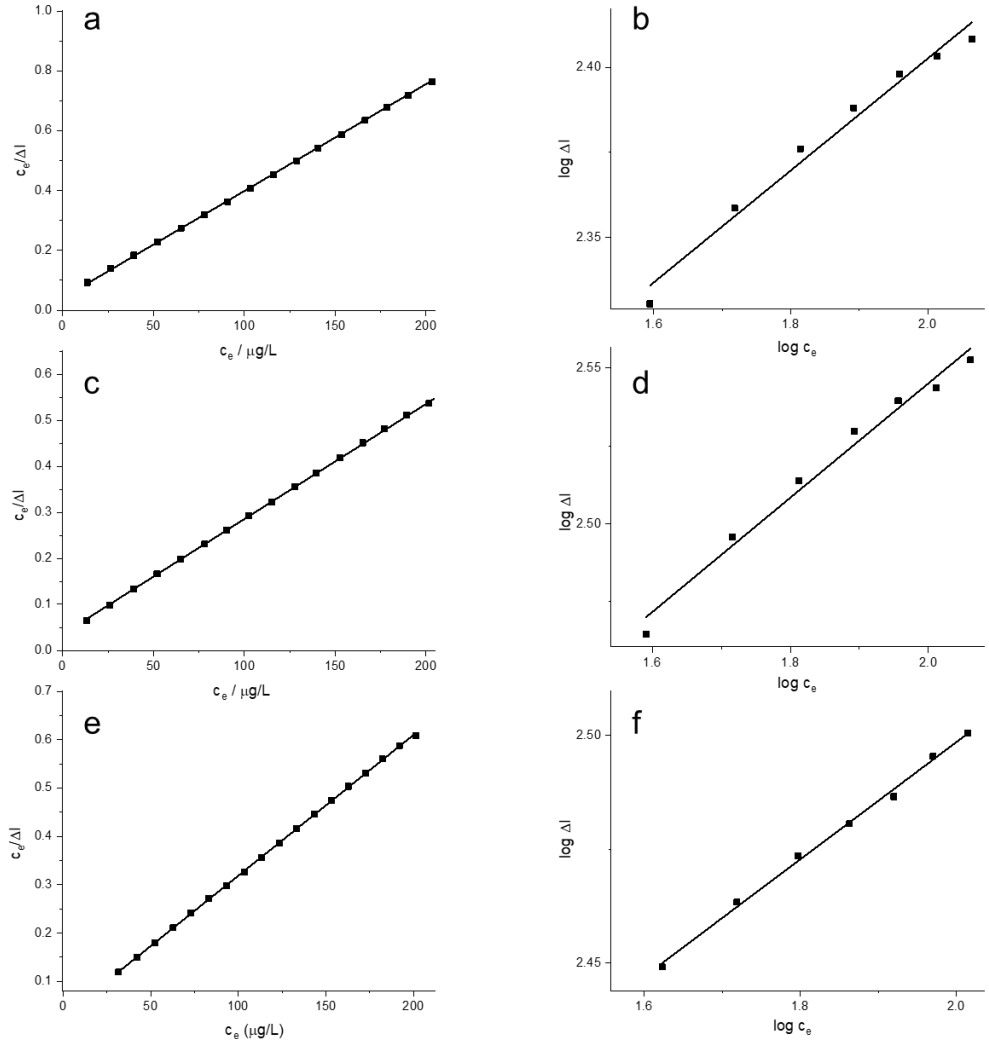

2

Fig. 8 Langmuir adsorption isotherms for (a) Cd^{2+}, (c) Cu^{2+} and (e) Pb^{2+} in the range of 13 – 202 mg dm^{-3}. Freundlich adsorption isotherms for (b) Cd^{2+}, (d) Cu^{2+} and (f) Pb^{2+}in the range 40 – 124 mg dm^{-3}

According to Sigel et al., guanine contains imidazole and pyridine-type nitrogens well suited for divalent metal ions binding [5], and in general the binding of metal cations is governed by the formation of energetically favorable coordination complexes [6], the interaction of guanine or a guanine derivative G with a divalent metal ion M^{2+} yields $M(G)^{2+}$ complexes [32]. Most investigations about the complexation of the nucleobases with metal ions do not focus on the free nucleobases, but rather on DNA itself or DNA-resembling structures and related bio-molecules [4]. Nonetheless, it is reported that amongst divalent metal ions that can bind both the phosphate and the DNA base, copper (II) has the strongest affinity to the base [6], which confirms our findings. It was shown that copper can be coordinated to guanine through the N(7) and O(6) atoms, as well as a possible mono-coordination to the N(7) position only, depending on the guanine tautomer [33]. Lead on the other hand is known to weakly interact with the N(7) and O(6) atoms of guanine [6] knowing that Pb^{2+} is an excellent oxidizer and strong Lewis acid [34]. Cadmium is classified as a soft metal that binds preferentially to DNA bases more than DNA phosphates. Notwithstanding the different studies dedicated to the interaction between Cd^{2+} and

nucleobases, the exact nature of binding remains uncertain. It was suggested that cadmium most likely binds to guanine at its N(7) center in a 1:1 ratio [35].

Comparing the behavior of the three divalent heavy metals with guanine, it is evident that the highest adsorption capacity is observed for Cu (II) followed by Pb (II) and Cd (II). This trend comes in accordance with a study done by Hammud et al. on the interaction of some nucleobase derivatives with divalent metals. They found that it follows the ionic radii of the cations such that as the radius increases, the stability of the formed complexes increases [36]. This order is also in agreement with a report by Sharma et al. who potentiometrically studied the stability constant of a pyrimidine derivative with divalent metal ions. According to their observations, the trend depends on both the ionic radius and the second ionization energy [37]. Based on a recent study, different factors affect the stability of metal complexes including the nature of the central metal ion, nature of the ligand, chelating effect, macrocyclic effect, resonance effect and steric effect/hindrance [38]. Thus, this original and sensitive design can further help clarify the guanine-heavy metal interaction, with a possible application of these functionalized beads as advanced material for heavy metal ions complexation, removal and detection from aqueous solutions.

The effect of other divalent ions such as Ca^{2+} was tested. The SWV signal decreased less than 10% for high concentrations (>100mg/L), showing a very weak interaction.

Voltammetric detection of divalent heavy metals with the GH-APTES-Fe_3O_4 modified BDD electrode

Following the adsorption isotherms, the plots of each heavy metal were assessed to study the analytical behavior of the guanine hydrazide functionalized nanoparticles. Starting with cadmium in figure 9a, its plot can be divided into 2 linear parts: the first linear range was found between 0.232 and 0.809 µmol dm^{-3} with a correlation coefficient r^2 of 0.9274 and sensitivity of 101.4 µA $µmol^{-1}$ dm^3 while the second linear range was observed between 0.925 and 1.815 µmol dm^{-3} with r^2= 0.9775 and sensitivity of 13.4 µA $µmol^{-1}$ dm^3. Considering the first linear range, the obtained concentration range and limit of detection are comparable to reported values using Fe_3O_4 nanoparticles for the detection of Cd (II) by square wave voltammetry (Table 2).

Table 2 Comparison of the linear detection range and sensitivity with previously reported values for the electrochemical detection of Cd (II)

Electrode modification	**Method**	**Concentration Range (µmol dm^{-3})**	**LOD (µmol dm^{-3})**	**Sensitivity (µA µmol^{-1} dm^3)**	**Reference**
Polydopamine-Fe_3O_4	SWASV	0.02 – 0.59	9.2×10^{-5}	196	[39]
Reduced graphene oxide-Fe_3O_4	SWASV	0 – 0.8	0.056	14.82	[40]
Chitosan-Fe_3O_4	SWASV	1.2 – 1.7	0.0392	8.11	[1]
Fe_3O_4	SWASV	0.3 – 1.3	0.154	3.18	[41]
Terephthalic acid-Fe_3O_4	SWASV	0.4 – 1.1	0.2	12.15	[42]
GH-APTES-Fe_3O_4	SWV	0.232 – 0.809	0.077	101.4	Current work

The same behavior was noticed upon the subsequent addition of Pb (II) and Cu (II) respectively. The measurements were carried out in a citrate buffer solution pH 4. As shown in Fig. 9b, the calibration graph obtained for Pb (II) detection exhibited two linear response ranges of 0.0483 – 0.4521 µmol dm^{-3} (r^2 = 0.9113) and 0.550 - 1 µmol dm^{-3} (r^2= 0.98601) with the sensitivities of 156.38 µA µmol^{-1} dm^3 and 28.25 µA µmol^{-1} dm^3, respectively. By comparing the results obtained with previously reported

electrochemical studies, a noticeable increase in sensitivity, similar to the case of Cd (II) was noticed (Table 3).

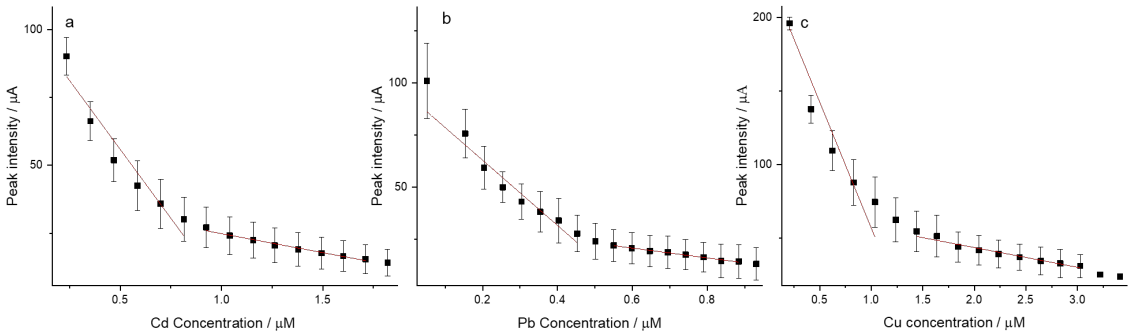

Fig. 9 Linear ranges of (a) cadmium, (b) lead and (c) copper at the GH-APTES-Fe_3O_4 NP electrode

Table 3 Comparison of the current concentration range and sensitivity with previously reported values for the electrochemical detection of Pb (II)

Electrode modification	**Method**	**Concentration Range (µmol dm^{-3})**	**LOD (µmol dm^{-3})**	**Sensitivity (µA µmol^{-1} dm^3)**	**Reference**
Amine–Fe_3O_4	SWASV	0.5 – 8	0.15	10.07	[43]
Polydopamine-Fe_3O_4	SWASV	5×10^{-3} – 0.6	1.4×10^{-6}	235	[39]
Fe_3O_4	SWASV	0.3 – 1.3	0.119	14.9	[41]
Chitosan-Fe_3O_4	SWASV	0.1 – 1.3	0.0422	50.6	[1]
Terephthalic acid-Fe_3O_4	SWASV	0.4 – 1.1	0.04	8.56	[42]

GH-APTES-Fe_3O_4	SWV	0.0483 – 0.497	0.011	156	Current work

In the case of Cu (II), the calibration plots were divided between two linear ranges: the first range from 0.209 to 1.03 µmol dm^{-3} with r^2= 0.92098 and a sensitivity of 171.6 µA µmol^{-1} dm^3, and the second range from 1.44 to 3 µmol dm^{-3} with r^2= 0.94262 and a sensitivity of 13.5 µA µmol^{-1} dm^3. It is worth mentioning that the sensitivity for copper is much higher (more than ten folds) than in all other reported works using iron oxide nanoparticles [3, 11, 1, 41] with a comparable limit of detection of 0.069 µmol dm^{-3}.

Furthermore, the reproducibility among five independent GH functionalized Fe_3O_4 electrodes was evaluated by comparing the linear ranges with each of the studied heavy metals. The data in figure 9 show that the electrochemical sensor demonstrates a good reproducibility over five independent measurements such that the maximum relative standard deviation RSD is 4% in the case of Cu (II), 5% for Pb (II) and 10% for Cd (II).

Conclusion

In the present work, we report the development of a novel material, GH-APTES functionalized iron oxide nanoparticles. These nanoparticles were used to modify a BDD electrode in order to assess the interaction between guanine hydrazide and divalent heavy metal ions. The adsorption

isotherms were investigated and it was proven that the data are better modelled with Langmuir isotherm, with adsorption capacities decreasing in the order: $Cu^{2+}>Pb^{2+}>Cd^{2+}$. This design allowed us to evaluate these ions such that the sensitivities and LODs were 171.61 μA μmol^{-1} dm^3 and 0.069 μmol dm^{-3} for Cu (II), 156 μA μmol^{-1} dm^3 and 0.0161 μmol dm^{-3} for Pb (II) and 101.4 μA μmol^{-1} dm^3 for 0.077 μmol dm^{-3} Cd (II), respectively. Moreover, the sensitivity obtained in the detection of copper was at least ten times greater than all reported sensitivities using iron oxide. We anticipate that the synthesized GH-APTES-Fe_3O_4 nanoparticles are promising materials that can be used rapidly and economically for heavy metal complexation and removal for water decontamination. Further tests utilizing the different hydrazide nucleobases derivatives for the detection of heavy metals could be of interest and could help better elucidate the sensitivity and the mechanism of interaction between nucleobases and heavy metal ions.

Experimental

Chemical Reagents

All the reagents used in this study were of analytical grade and used as received without any further purification. Ammonium hydroxide (NH_4OH) (25% in H_2O), (3-aminopropyl)triethoxysilane (APTES) 99%, glutaraldehyde solution Grade II (25% in H_2O), potassium chloride (99 – 100.5%) and potassium citrate tribasic monohydrate (≥ 99%) were

purchased from Sigma-Aldrich. Dimethyl sulfoxide (DMSO) (≥ 99.9%) was purchased from Riedel-de-Haën, sodium hydroxide (NaOH) (98.5 – 100%), cadmium, copper and lead standards from Fluka and ethanol (≥ 99.8%) from Honeywell. Ferric chloride hexahydrate $FeCl_3.6H_2O$ (98%) and ferrous chloride tetrahydrate $FeCl_2.4H_2O$ (99%) were purchased from Acros Organic. All the chemicals used in the synthesis and characterization of guanine hydrazide were purchased from Sigma-Aldrich, Merck or Fluka Chemika. Deionized water (with a resistivity of 18.2 MΩ.cm) was used in the preparation of all solutions.

Synthesis and characterization of guanine hydrazide

A round bottom flask was charged with guanine (10 g, 66.22 mmol) *N*,*N*-dimethylacetamide (DMA, 30 cm^3) and acetic anhydride (16.5 cm^3, 168 mmol). The reaction mixture was stirring overnight at 165°C after which it was cooled to room temperature. The precipitate was collected and triturated with water/ethanol 1:1 (30 cm^3) at 80°C for 2-3 h. The precipitate was collected and dried under reduced pressure at 70°C to yield a white solid. The solid was transferred to a 500 cm^3 round bottom flask with dimethylformamide (50 cm^3). An ethanolic solution of sodium ethoxide (NaOEt, 2 cm^3, 25.9 mmol) was added and the mixture was stirred for 15 min. Ethyl acrylate (3.8 cm^3, 34.96 mmol) was added and the mixture was refluxed at 165°C for 1h. The solvent was evaporated and the residue was

dissolved in methylene chloride and washed with distilled water. The organic layer was separated, dried with anhydrous $MgSO_4$, filtered and the solvent evaporated under reduced pressure. The crude was then triturated with toluene (250 cm^3) with stirring overnight at room temperature. The precipitate was collected, dried under reduced pressure and purified by column chromatography on silica gel (CH_2Cl_2/MeOH 98:2) to yield a white solid (2.85 g). The white solid (7 g, 23.9 mmol) was mixed with ethanol (70 cm^3) and $N_2H_4.H_2O$ (4.1 cm^3, 83.6 mmol) and the mixture was stirred and heated at 80°C for 24 h. The precipitate was collected and dried at 70°C under reduced pressure to yield a white solid. ^1H and ^{13}C nuclear magnetic resonance (NMR) spectra were recorded on a Bruker 300 MHz NMR spectrometer in DMSO, $CDCl_3$ and D_2O or D_2O/D_2SO_4, using TMS and DSS as references; chemical shifts are reported in ppm. Fourier Transform Infrared (FTIR) spectra were collected using PerkinElmer Spectrum Two spectrometer.

Fabrication of APTES-coated iron oxide nanoparticles

Magnetic nanoparticles were synthesized according to a modified Massart's method [20] based on coprecipitation of an aqueous mixture of ferric and ferrous salt hydrates followed by the addition of a base. Briefly, 2.7 g of $FeCl_3.6H_2O$ and 1.2 g of $FeCl_2.4H_2O$ were mixed with a molar ratio of 2:1 and dissolved in 90 cm^3 of deionized water. Afterwards, 100 cm^3 of 1

mol dm^{-3} NaOH solution was added dropwise under vigorous stirring and nitrogen gas at 0°C. A change in color indicated the formation of iron oxide nanoparticles. The solution was subjected to magnetic stirring for 4 hours to ensure nucleation and growth of magnetite nanoparticles. The latter were collected with an external magnet, washed several times with water followed by ethanol, and finally dried under vacuum. The solution was subjected to magnetic stirring for 60 minutes to ensure nucleation and growth of magnetite particles. APTES coating was carried out afterwards. Iron oxide nanoparticles were sonicated for 25 minutes before the addition of NH_4OH and (3-aminopropyl)triethoxysilane under nitrogen atmosphere. The mixture was allowed to age for 24 hours, after which the nanoparticles were again washed with water followed by ethanol and dried for later use.

Characterization of iron oxide nanoparticles coated with APTES

FTIR spectra were collected at each step of the synthesis using PerkinElmer Spectrum Two spectrometer in order to verify the successful synthesis of the APTES coated magnetic nanoparticles. In order to identify the crystalline phase of the prepared nanoparticles, X-ray diffraction (XRD) was performed using a Bruker D4 ENDEAVOR with Cu/K-α radiation. The operating target voltage was 50 kV and the tube current was 50 mA. The morphology and size of the nanoparticles were investigated using Scanning

Electron Microscopy (SEM) done using Tescan, Vega 3 LMU with Oxford EDX detector (Inca XmaW20).

Fabrication of the electrochemical sensor

Guanine hydrazide was immobilized on the APTES coated iron oxide nanoparticles using glutaraldehyde (GA) as a crosslinking agent. Briefly, a 1 mg/mL solution of GH dissolved in DMSO was mixed with 100 mg dm^{-3} of the APTES coated nanoparticles. 20 mm^3 of this mixture were dropped on a clean BDD electrode and left for 20 minutes in saturated glutaraldehyde vapor. The electrode was left to dry at room temperature. Afterwards, it was placed on the electrochemical cell where a 300 mT cylindrical magnet will permit the paramagnetic nanoparticles to remain attracted to the electrode's surface.

Electrochemical measurements

All electrochemical measurements were performed using a PalmSens4. A conventional three-electrode system was employed: a bare or modified boron doped diamond electrode as the working electrode, Platinum plate as a counter electrode and Ag/AgCl as a reference electrode. Citrate buffered solutions (0.1 mol dm^{-3}, containing 0.5 mol dm^{-3} KCl, pH 4) were used as electrolytes for all electrochemical measurements. The technique used in all the measurements was square wave voltammetry with the

following optimized conditions: frequency 50 Hz; amplitude 50 mV; step potential 10 mV; time of equilibration 2 minutes.

Acknowledgements The authors acknowledge the financial support of the EU H2020 research and innovation program entitled Kardia Tool grant #768686.

References

1. Zhou SF, Han XJ, Liu YQ (2016) J Alloys Compd 684, 1-7
2. Toor SK, Devi P, Bansod BKS (2015) Aquatic Procedia 4, 1107–1113
3. Dedelaite L, Kizilkaya S, Incebay H, Ciftci H, Ersoz M, Yazicigil Z, Oztekin Y, Ramanaviciene A, Ramanavicius A (2015). Colloids Surf, A 483, 279–284
4. Zhan S, Wu Y, Wang L, Zhan X, Zhou P (2016) Biosens Bioelectron 86, 353-368.
5. Roland KO, Sigel HS (2010) Acc Chem Res 43(7), 974–984
6. Kanellis VG, Dos Remedios CG (2018) Biophys Rev 10(5), 1401-1414
7. Zhang XB, Kong RM, Lu Y (2011) Annu Rev Anal Chem 4, 105-128
8. Saidur MR, Aziz AR, Basirun WJ (2017) Biosens Bioelectron 90, 125-139.

9. Moriwaki H (2003) J Mass Spectrom. 38(3), 321-327

10. Burda JV, Šponer J, Šebesta F (2017) Handbook of Computational Chemistry https://doi.org/10.1007/978-3-319-27282-5_36

11. Subramanian P, Dryhurst G (1987) J Electroanal Chem 224(1-2), 137-162

12. Afkhami A, Moosavi R, Madrakian T, Keypour H, Ramezani-Aktij A, Mirzaei-Monsef M (2014) Electroanalysis 26(4), 786–795

13. Wang G, Ma Y, Tong Y, Dong X (2016) Smart Materials and Structures 25(3), 035028

14. Wu D, Li Y, Zhang Y, Wang P, Wei Q, Du B (2014) Electrochim Acta 116, 244–249

15. Khosroshahi ME, Ghazanfari L (2012) Mater Sci Eng, C 32(5), 1043–1049

16. Chen JP, Yang PC, Ma YH, Tu SJ, Lu YJ (2012) Int J Nanomedicine 7, 5137–5149

17. Yamaura M, Camilo RL, Sampaio LC, Macêdo MA, Nakamura M, Toma HE (2004) J Magn Magn Mater 279(2-3), 210–217

18. Yew YP, Shameli K, Miyake M, Ahmad Khairudin NBB, Mohamad SEB, Hara H, Mad Nordin MFB, Lee KX (2017) IEEE Trans Nanotechnol 16(6), 1047–1052

19. Swain GM, Ramesham R (1993) Anal Chem 65(4), 345–351

20. Bee RMA, Neveu S (1995) J Magn Magn Mater 149(1-2), 6–9

21. Pulido D, Sánchez A, Robles J, Pedroso E, Grandas A (2009) Eur J Org Chem 2009(9), 1398–1406

22. Karabanovich G, Zemanova J, Smutny T, Szekely R, Sarkan M, Centarova I, Vocat A, Pavkova I, Conka P, Nemecek J, Stolarikova J, Vejsova M, Vavrova K, Klimesova V, Hrabalek A, Pavek P, Cole ST, Mikusova K, Roh J (2016) J Med Chem 59(6), 2362–2380

23. Hammud HH, El-Dakdouki MH, Mohamd Sonji N, Bouhadir KH (2015) Eur J Chem *6*(3), 325-336

24. Prado C, Flechsig GU, Grundler P, Foord JS, Markenc F, Compton RG (2002) Analyst 127(3), 329–332

25. Sun H, Dong L, Yu H, Huo M (2013) Russ J Electrochem 49(9), 883–887

26. Senthil Kumar CVP, Kirthika K, Sathish Kumar K (2010) Brazilian Journal of Chemical Engineering 27(2), 339–346

27. Langmuir I (1918) J Am Chem Soc 40(9), 1361–1403

28. Subramanyan Vasudevan JL, Vanathi R (2010) Clean: Soil, Air, Water, 38(1), 9–16

29. Kumar KY, Raj TNV, Archana S, Prasad SBB, Olivera S, Muralidhara HB (2016) Journal of Water Process Engineering 13, 44–52

30. Fierro V, Torné-Fernández V, Montané D, Celzard A (2008) Microporous Mesoporous Mater 111(1-3), 276–284
31. Zhan W, Xu C, Qian G, Huang G, Tang X, Lin B (2018) RSC Adv 8(33), 18723–18733
32. Bin Song JZ, Sigel H, Griesser R, Meiser C, Lippert B (1999) Chem Eur J 5(8), 2374–2387
33. Marino T, Toscano M, Russo N, Grand A (2004) Int J Quantum Chem 98(4), 347–354
34. Dimkovikj A, Banton MJ, McDanel LA, Arndt KN, Unvert KE, Thorn EK, Marco AR, Hellmann-Whitaker RA (2017) J Inorg Biochem 171, 90–99
35. Hossain Z, Huq F (2002) J Inorg Biochem 90(3-4), 97–105
36. Hammud HH, M.H. El-Dakdouki, N. Sonji, G. Sonji, Bouhadir KH (2016) Nucleosides, Nucleotides Nucleic Acids 35(5), 259–276
37. Sharma P, Swaika B, Millal S, Sharma RK, Sindhwani SK (2001) Indian J Chem, Sect A: Inorg, Bio-inorg, Phys, Theor Anal Chem. Vol. 40A, 1076-1081
38. Muthaiah S, Bhatia A, Kannan M (2020) Intech Open. DOI: 10.5772/intechopen.90894
39. Song Q, Li M, Huang L, Wu Q, Zhou Y, Wang Y (2013) Anal Chim Acta 787, 64–70

40. Sun YF, Chen WK, Li WJ, Jiang TJ, Liu JH, Liu ZG (2014). J Electroanal Chem 714-715, 97–102

41. Fan HL, Zhou SF, Gao J, Liu YZ (2016) J Alloys Compd 671, 354–359

42. Deshmukh S, Kandasamy G, Upadhyay RK, Bhattacharya G, Banerjee D, Maity D, Deshusses MA, Roy SS (2017) J Electroanal Chem 788, 91–98

43. Xiong S, Wang M, Cai D, Li Y, Gu N, Wu Z (2013) Anal Lett 46(6), 912–922

Figure Captions

Fig. 1 Schematic diagram showing the steps of guanine hydrazide synthesis

Fig. 2 (a) FTIR spectrum, (b) ^{1}H NMR (c) ^{13}C NMR and (d) HRMS of guanine hydrazide

Fig. 3 Schematic diagram showing the process of synthesizing the GH-APTES-Fe_3O_4 nanoparticles

Fig. 4 (A) FTIR spectrum of (a) bare Fe_3O_4 NPs, (b) APTES- Fe_3O_4 NPs and (c) GH-APTES-Fe_3O_4 NPs, (B) XRD pattern, (C) SEM image and (D) EDX spectrum of APTES-Fe_3O_4 nanoparticles

Fig. 5 SWV of (a) APTES-Fe_3O_4 nanoparticles and (b) APTES-Fe_3O_4 nanoparticles functionalized with GH

Fig. 6 Oxidation reaction of guanine, in aqueous medium

Fig. 7 SWV of (a) Cd (II) at the GH-APTES-Fe_3O_4 NP electrode over a concentration range of 0 – 2.5 μmol dm^{-3}, (b) Pb (II) at the GH-APTES-Fe_3O_4 NP electrode over a concentration range of 0 – 1 μmol dm^{-3} and (c) Cu (II) at the GH-APTES-Fe_3O_4 NP electrode over a concentration range of 0 – 3.5 μmol dm^{-3}

Fig. 8 Langmuir adsorption isotherms for (a) Cd^{2+} in the range of 13 – 265 mg dm^{-3}, (c) Cu^{2+} in the range of 13 – 229 mg dm^{-3} and (e) Pb^{2+} in the range of 5 – 202 mg dm^{-3}. Freundlich adsorption isotherms for (b) Cd^{2+} in the range 40 – 142 mg dm^{-3}, (d) Cu^{2+} in the range 26 – 130 mg dm^{-3} and (f) Pb^{2+} in the range 31 – 124 mg dm^{-3}

Fig. 9 Linear ranges of (a) cadmium, (b) lead and (c) copper at the GH-APTES-Fe_3O_4 NP electrode

Table 1 Constant parameters and correlation coefficients calculated for different adsorption models for Cu^{2+}, Cd^{2+} and Pb^{2+} adsorption

Isotherm	**Langmuir**				**Freundlich**		
Constants	Q_0 (µg g^{-1})	b (L μg^{-1})	R_L	r^2	n	k_F (µg.g^{-1})	r^2
Cd^{2+}	280.1	0.087	0.0394	0.9999	6.06	118.2	0.9614
Cu^{2+}	400	0.0707	0.0341	0.9998	5.447	150.7	0.9796
Pb^{2+}	343.6	0.1046	0.0271	0.9999	7.776	174.3	0.9961

Table 2 Comparison of the linear detection range and sensitivity with previously reported values for the electrochemical detection of Cd (II)

Electrode modification	**Method**	**Concentration Range (µmol dm^{-3})**	**LOD (µmol dm^{-3})**	**Sensitivity (µA μmol^{-1} dm^3)**	**Reference**
Polydopamine-Fe_3O_4	SWASV	0.02 – 0.59	9.2×10^{-5}	196	[39]
Reduced graphene oxide-Fe_3O_4	SWASV	0 – 0.8	0.056	14.82	[40]
Chitosan-Fe_3O_4	SWASV	1.2 – 1.7	0.0392	8.11	[1]
Fe_3O_4	SWASV	0.3 – 1.3	0.154	3.18	[41]

Terephthalic acid-Fe_3O_4	SWASV	0.4 – 1.1	0.2	12.15	[42]
GH-APTES-Fe_3O_4	SWV	0.232 – 0.809	0.077	101.4	Current work

1

2

3 **Table 3** Comparison of the current concentration range and sensitivity with

4 previously reported values for the electrochemical detection of Pb (II)

Electrode modification	**Method**	**Concentration Range (µmol dm^{-3})**	**LOD (µmol dm^{-3})**	**Sensitivity (µA $µmol^{-1}$ dm^3)**	**Reference**
Amine–Fe_3O_4	SWASV	0.5 – 8	0.15	10.07	[43]
Polydopamine-Fe_3O_4	SWASV	5×10^{-3} – 0.6	1.4×10^{-6}	235	[39]
Fe_3O_4	SWASV	0.3 – 1.3	0.119	14.9	[41]
Chitosan-Fe_3O_4	SWASV	0.1 – 1.3	0.0422	50.6	[1]
Terephthalic acid-Fe_3O_4	SWASV	0.4 – 1.1	0.04	8.56	[42]
GH-APTES-Fe_3O_4	SWV	0.0483 – 0.497	0.011	156	Current work

5

6

1 *Figure 1*

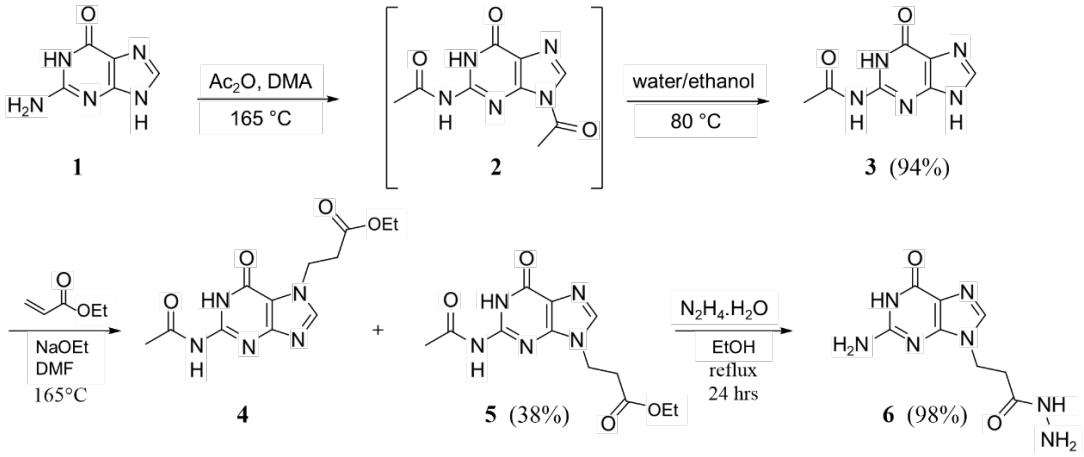

2

3 *Figure 2*

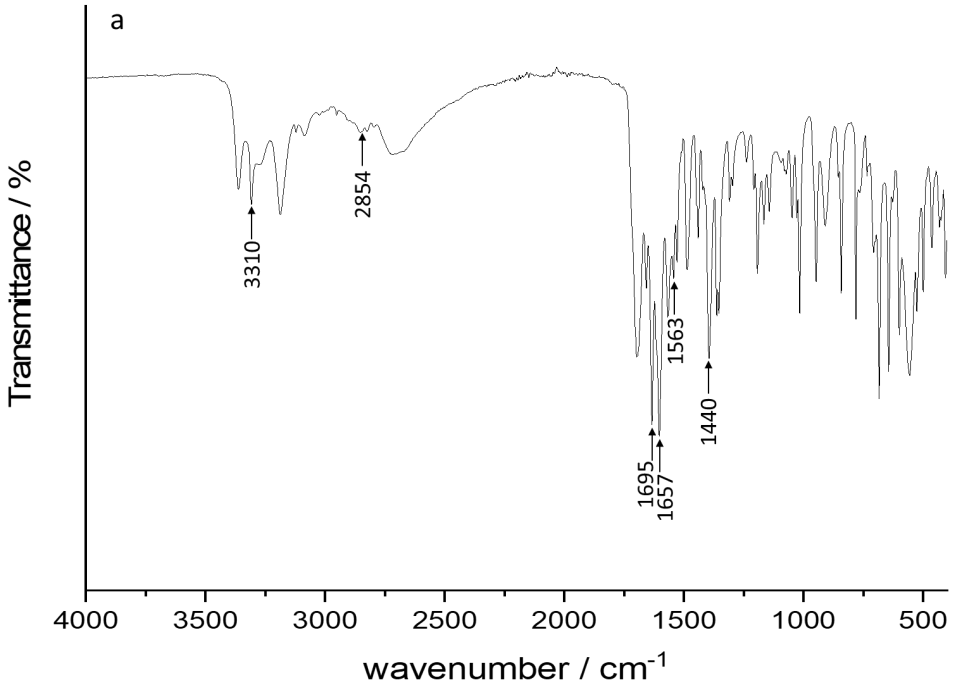

4

1

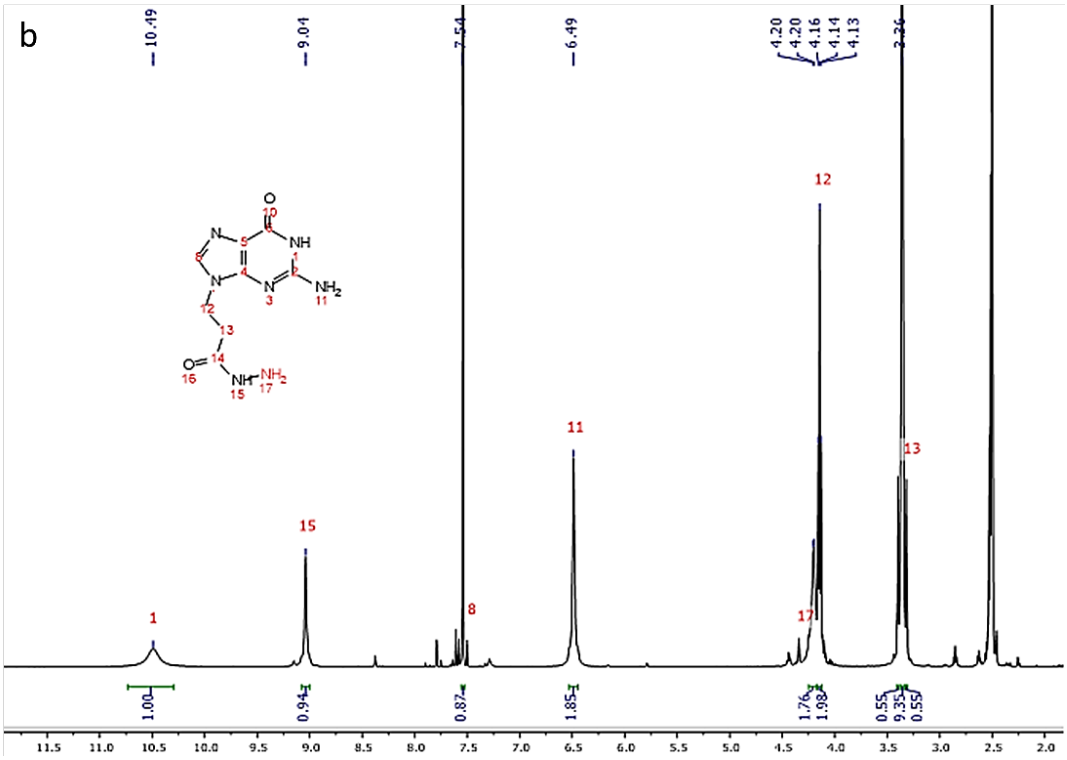
b
10.49
9.04
7.54
6.49
4.20
4.20
4.16
4.14
4.13
3.36
1.00
0.94
0.87
1.85
1.76
1.98
0.55
9.35
0.55

2

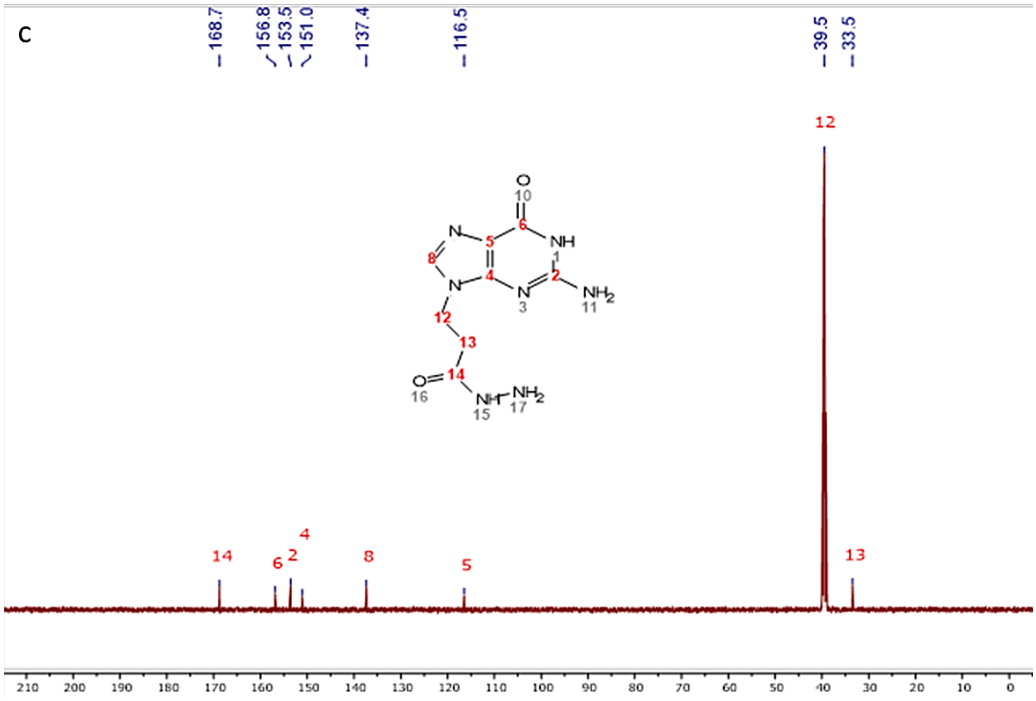
c
168.7
156.8
153.5
151.0
137.4
116.5
39.5
33.5

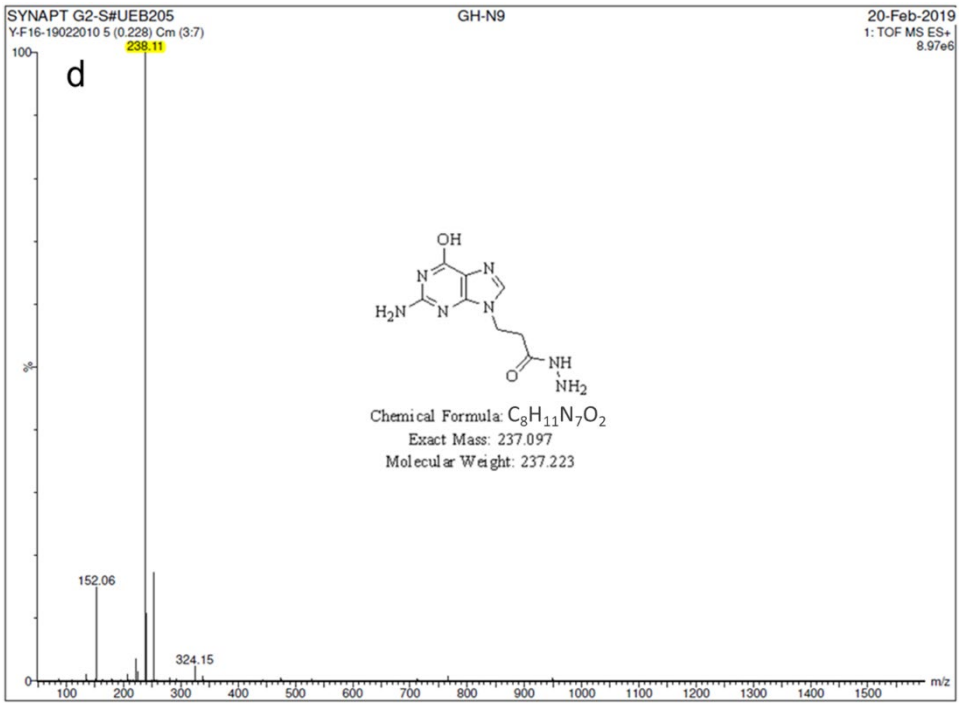

Figure 3

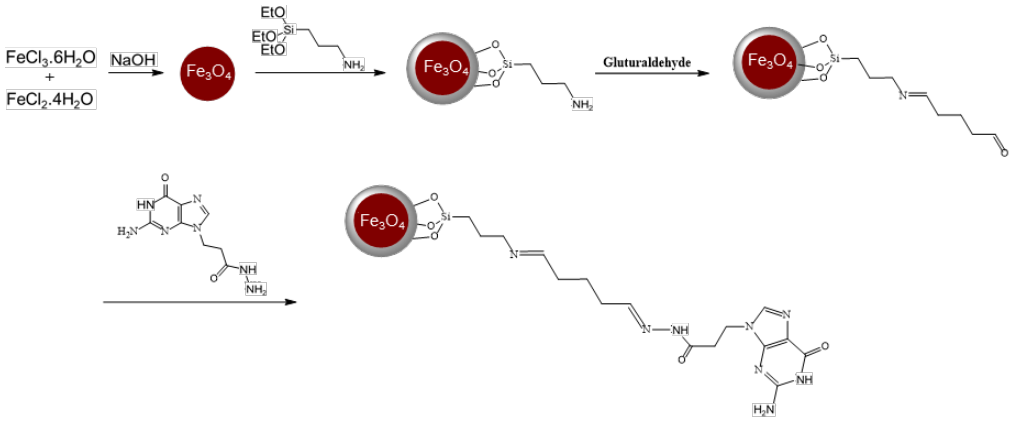

Figure 4

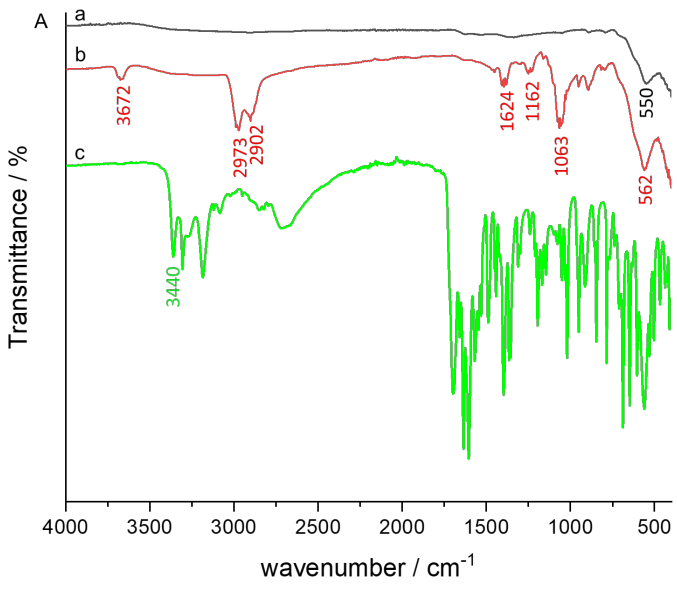
A
a
b
c
3672
2973
2902
1624
1162
1063
550
562
3440
Transmittance / %
4000
3500
3000
2500
2000
1500
1000
500
wavenumber / cm-1

1

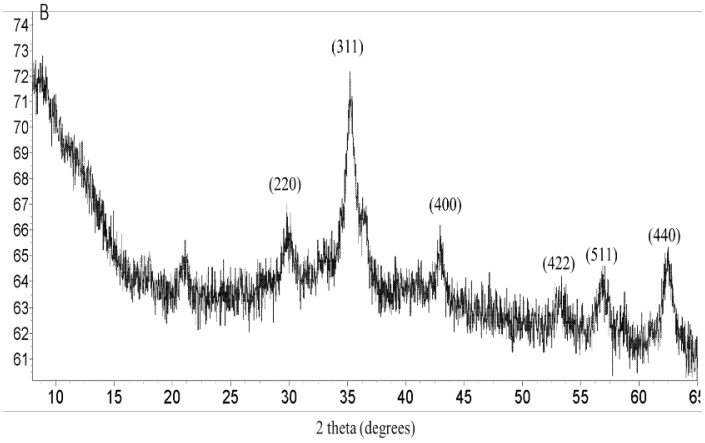
B
(311)
(220)
(400)
(422)
(511)
(440)
2 theta (degrees)

2

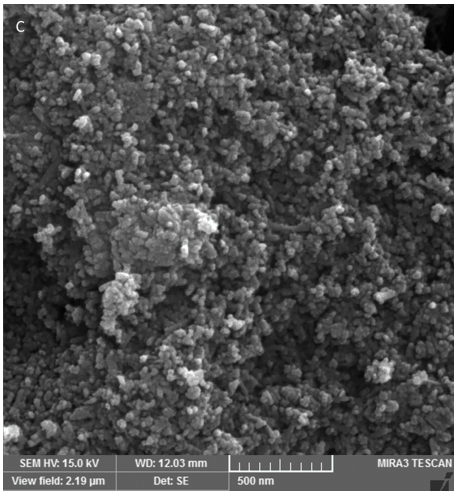
C
SEM HV: 15.0 kV
WD: 12.03 mm
MIRA3 TESCAN
View field: 2.19 µm
Det: SE
500 nm

3

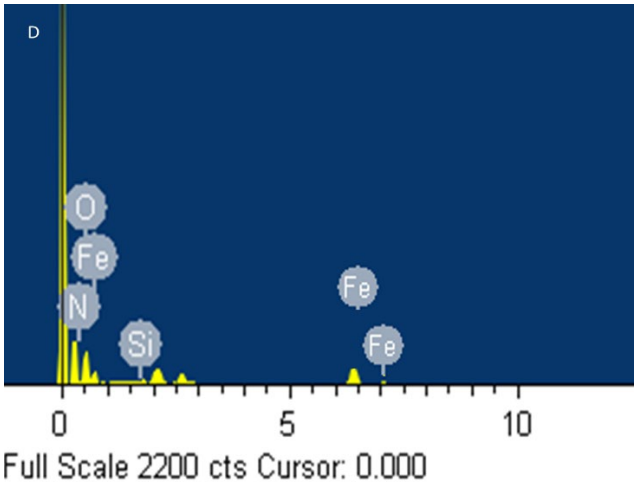

Figure 5

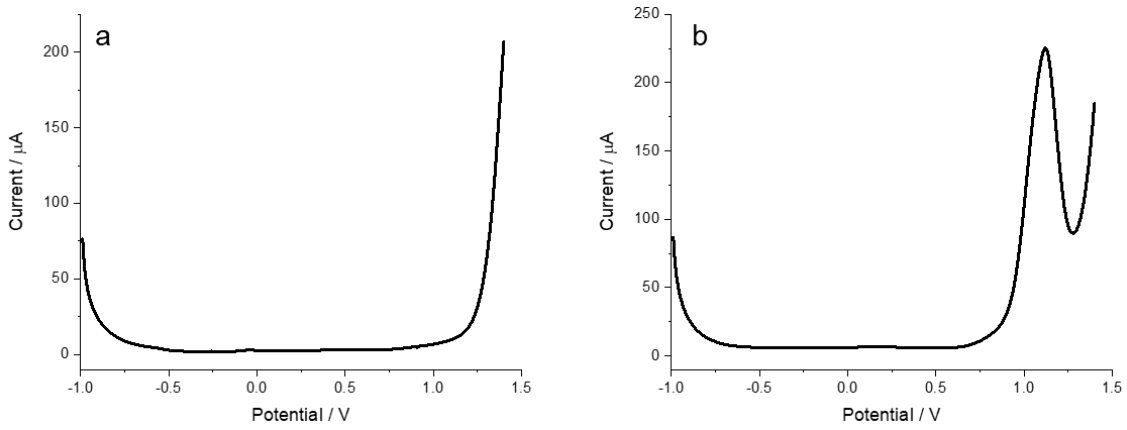

Figure 6

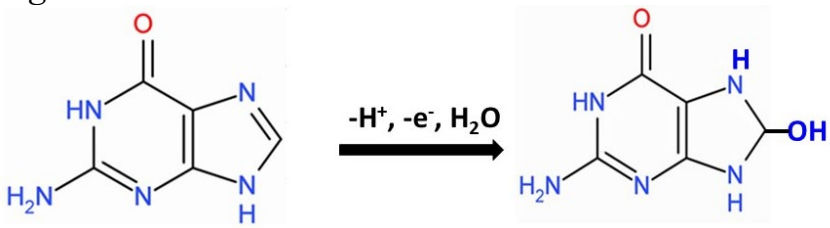

Figure 7

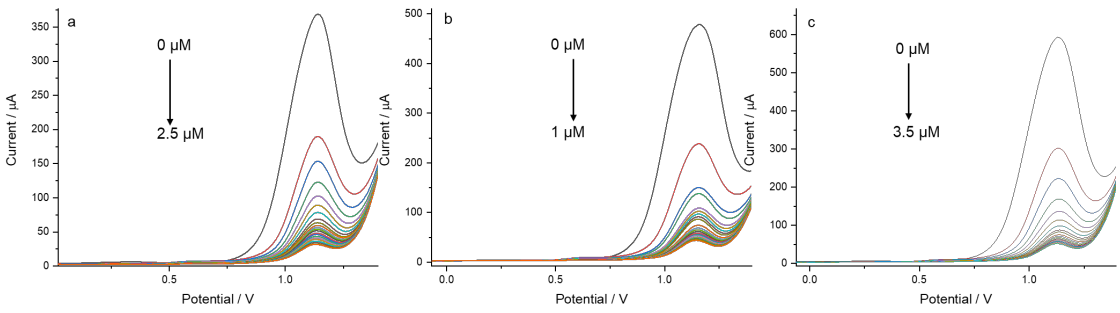

1 *Figure 8*

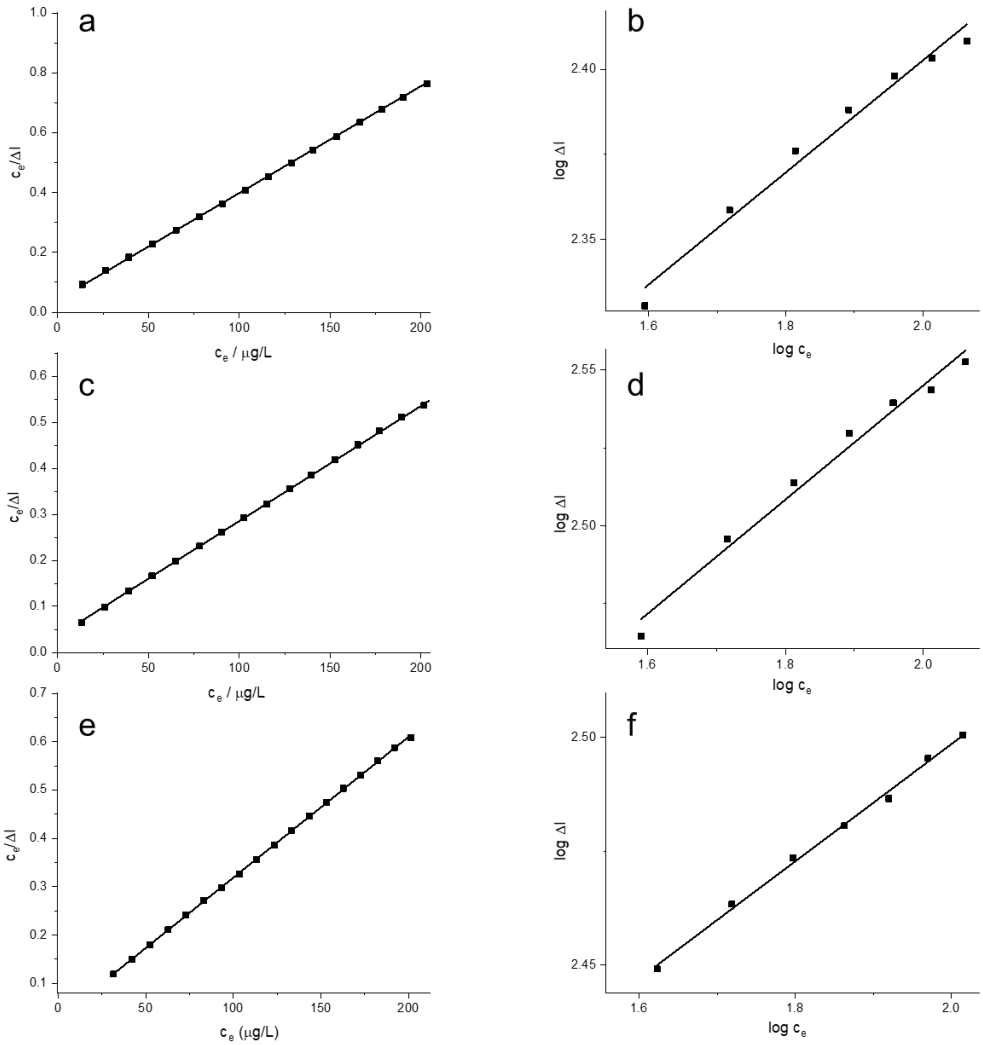

2
3
4 *Figure 9*

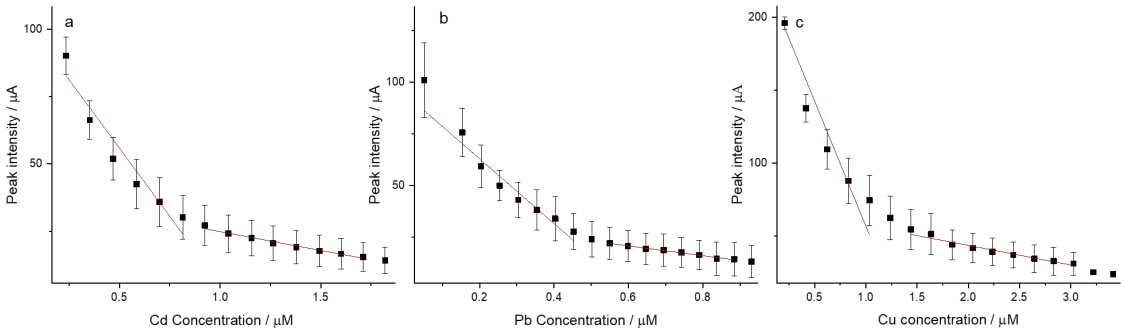

5
6

1 Graphical abstract

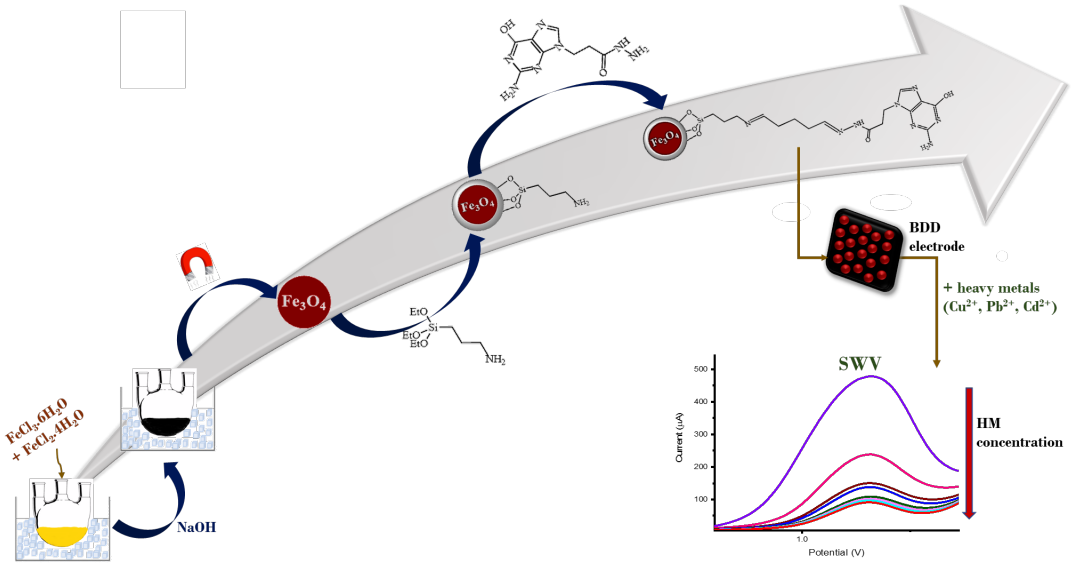

2